Numerical Study of Vortex Shedding Control Using Viscoelastic Flow Over an Elliptical Cylinder

Annisa Dwi Sulistyaningtyas[1], Basuki Widodo[2], Chairul Imron[2], and Hanim Faizah[4]

***Abstract*—Vortex-Induced Vibration (VIV) mitigation is a critical issue in engineering systems involving bluff bodies subjected to fluid flow. This study presents a numerical investigation of viscoelastic fluid flow over an elliptical cylinder as a passive control strategy to suppress vortex shedding. The governing continuity, momentum, and energy equations for an incompressible viscoelastic fluid are formulated and solved using an implicit finite difference method. The viscoelastic behavior of the fluid is incorporated through a nonlinear constitutive model, and the resulting system of equations is transformed into a dimensionless form to facilitate analysis. The study focuses on the effects of key parameters, including the viscoelastic parameter K, the Prandtl number Pr, and the geometric aspect ratio a/b of the elliptical cylinder. Numerical simulations are performed using MATLAB to evaluate the resulting velocity and temperature distributions within the boundary layer region. The results indicate that increasing the viscoelastic parameter significantly reduces the peak velocity near the wall and weakens the velocity gradient, leading to a decrease in shear stress. In addition, higher viscoelasticity contributes to a thicker momentum and thermal boundary layer, which reduces the rate of heat transfer from the surface. Furthermore, variations in the Prandtl number and aspect ratio are found to influence the localization of thermal and momentum transport. Higher values of Pr result in thinner thermal boundary layers and enhanced temperature gradients near the surface, while changes in a/b primarily affect the near-wall flow structure. Overall, the combined effects of viscoelasticity and geometric modification demonstrate a strong potential for attenuating vortex shedding and reducing the likelihood and intensity of VIV. These findings provide valuable insights for the design of engineering systems involving non-Newtonian fluids and flow-induced vibrations.**

Keywords: Vortex-Induced Vibration, Numerical Simulation, Matlab, Viscoelastic Fluid, Elliptical Cylinder

*This work was not supported by any organization

[1]Annisa Dwi Sulistyaningtyas is with Faculty of Teacher Training and Education, Mathematics Education, Universitas PGRI Adi Buana Surabaya, Surabaya, 60234, Indonesia annisadwistyas@unipasby.ac.id

[2]Basuki Widodo is with the Department of Mathematics, Sepuluh Nopember Institute of Technology, Surabaya, 60111, Indonesia b.widodo@matematika.its.ac.id

[3]Chairul Imron is with the Department of Mathematics, Sepuluh Nopember Institute of Technology, Surabaya, 60111, Indonesia imron-its@matematika.its.ac.id

[4]Hanim Faizah is with Faculty of Teacher Training and Education, Mathematics Education, Universitas PGRI Adi Buana Surabaya, Surabaya, 60234, Indonesia fhanim@unipasby.ac.id

Manuscript received January 22, 2026; accepted May 19, 2026.

NOMENCLATURE

Dimensional Variables

x, y	spatial coordinates (m)
u, v	velocity components in x and y directions (m/s)
U_∞	free-stream velocity (m/s)
T	fluid temperature (K)
T_∞	ambient temperature (K)
T_w	wall temperature (K)
P	pressure (Pa)
ρ	fluid density (kg/m^3)
ν	kinematic viscosity (m^2/s)
k	thermal conductivity (W/m·K)
C_p	specific heat at constant pressure (J/kg·K)
α	thermal diffusivity (m^2/s)
Q_0	volumetric heat generation coefficient (W/m^3)
q_w	surface heat flux (W/m^2)
g	gravitational acceleration (m/s^2)
β	thermal expansion coefficient (1/K)
k_0	viscoelastic material parameter

Stress Components

τ_{xx}, τ_{yy}	normal stress components (Pa)
τ_{xy}, τ_{yx}	shear stress components (Pa)

Geometric Parameters

a	semi-axis normal to flow (m)
b	semi-axis along flow (m)
A	angle between surface normal and vertical axis
B	geometric angle parameter

Dimensionless Variables

θ	dimensionless temperature $(T - T_\infty)/(T_w - T_\infty)$
θ_w	dimensionless wall temperature
ψ	stream function
f	dimensionless stream function
η	similarity variable

Dimensionless Parameters

K	viscoelastic parameter
Pr	Prandtl number
Re	Reynolds number
We	Weissenberg number

Operators

∇	gradient operator
∂	partial derivative operator

I. INTRODUCTION

THE interaction between fluid flow and bluff bodies often gives rise to wake formation and vortex shedding, which in turn can generate significant fluctuating drag and lift forces. In engineering applications, ranging from offshore structures, risers, and subsea pipelines to industrial piping systems, the hydrodynamic and thermal loads arising from this interaction become critical factors for the stability, reliability, and service life of the structures. Therefore, a thorough understanding of the flow characteristics around bluff bodies is essential for safe and efficient design [1], [2].

In line with industrial developments and the need for specialized applications, such as the transport of polymer solutions, heavy oil, and drilling muds, many working fluids are non-Newtonian, in particular viscoelastic fluids [16]. This class of fluids exhibits a combined viscous and elastic character: in addition to shear stresses causing energy dissipation, the fluid can also store elastic energy and display stress-memory effects as well as normal stress differences. These characteristics can significantly alter the flow behaviour compared with Newtonian fluids, for example in terms of wake stability, stress distribution, and the flow response to disturbances [3].

However, with the growing use of complex fluids in industry—such as polymer suspensions, heavy oils, drilling muds, and other non-Newtonian fluids—attention to viscoelastic fluids has also increased. Viscoelastic fluids possess a combination of viscous and elastic properties, including the ability to store elastic energy, deformation memory effects, and normal stress differences, which can fundamentally alter the flow behaviour compared with Newtonian fluids [4]. In the context of flow around bluff bodies, fluid elasticity has the potential to modify wake structure, flow stability, and the distribution of stress and temperature. Several numerical studies have shown that viscoelastic models can exhibit flow and stress behaviours that differ significantly from those of Newtonian flows [6], [13], [14].

Research on how viscoelastic fluid properties can be used to prevent VIV in cylinders has also been carried out by [6]. In that study, a two-dimensional unsteady CFD simulation was performed by coupling the flow with the Finite Extensible Nonlinear Elastic-Peterlin (FENE-P) constitutive equation and the structural motion through Fluid-Structure Interaction (FSI). Relevant studies related to the present work have also been conducted by [7], [10], [13], [17]. The resulting mathematical model is solved numerically using several numerical methods, including the implicit Crank–Nicolson finite difference scheme, the explicit finite difference scheme, and other numerical techniques. Subsequently, the simulations are carried out using MATLAB software [8], [9], [11], [12], [15].

From the background problems described above, the present study focuses on a Numerical Study of Vortex Shedding Control Using Viscoelastic Flow Over an Elliptical Cylinder. This research can contribute as a basis for the design of industrial devices in sectors such as offshore engineering, oil and gas, subsea pipelines, heat exchangers, and industrial piping systems, which are highly susceptible to VIV. In addition, this study contributes to the modelling and numerical analysis of non-Newtonian fluid flow around bluff bodies by solving a coupled system of continuity, momentum, and energy equations for a viscoelastic fluid using an implicit finite difference scheme.

II. RESEARCH METHOD

A. Physical Model

This study employs a numerical simulation approach to analyse the velocity and temperature profiles of viscoelastic flow past an elliptical cylinder. The approach is based on computational fluid dynamics (CFD), using an implicit finite difference method to solve the flow and energy equations.

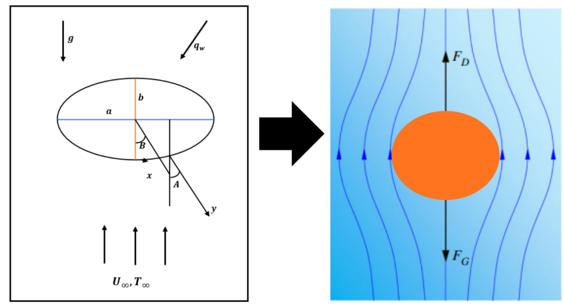

Fig. 1: Physical model of viscoelastic fluid flow past an elliptical cylindrical surface

In Figure 1, it can be seen that the fluid flows upward with a free-stream velocity U_∞ and is influenced by gravity as well as the ambient temperature T_∞. Because the viscoelastic effects of the fluid are dominant, the analysis is carried out in the boundary-layer region of the elliptic cylinder, namely in the lower stagnation region ($x \approx 0$). The fluid flows past an elliptic cylinder with semi-axis length a (normal to the fluid flow) and semi-axis length b (aligned with the fluid flow). In this coordinate system, A denotes the angle formed between the outer normal to the cylinder surface and the vertical line at the lower curved part of the cylinder, and B denotes the angle formed between the axis b and the normal line associated with the angle A. In addition, the flow is also subjected to a constant heat flux q_w.

B. Governing Equation

In this study, several governing equations are used to construct the mathematical model of viscoelastic fluid flow past an elliptic cylinder. The governing equations employed are the continuity equation, the momentum equation, and the energy equation. These equations are outlined in the following subsections.

Continuity Equation

In this study, it is also assumed that the flow is incompressible, i.e. the density ρ is constant, and steady state condition, so that the continuity equation is obtained in the following form.

$$\nabla \cdot \mathbf{V} = 0 \tag{1}$$

In scalar form, Eq. (1) can be written as follows:

$$\frac{\partial u}{\partial x} + \frac{\partial v}{\partial y} = 0 \tag{2}$$

Momentum Equation

This study also employs the momentum equation to develop the mathematical model, which is given as follows.

$$\frac{\partial\rho}{\partial t}\mathbf{V}+\rho(\mathbf{V}\cdot\nabla)\mathbf{V}=F_p+F_k+F_g \tag{3}$$

In this study, it is assumed that the fluid flow is in a steady state condition, that is, the flow does not depend on time. ($\frac{\partial\rho}{\partial t}=0$) and the fluid flow is also assumed to be incompressible, i.e. the density ρ is constant, so that we obtain

$$\rho(\mathbf{V}\cdot\nabla)\mathbf{V}=F_p+F_k+F_g \tag{4}$$

With F_p denoting the pressure force acting on the control volume, F_k the viscous force acting on the control volume, and F_g the gravitational force acting on the control volume, the scalar form of the momentum equation in the x- and y-directions is obtained as follows:

$$\rho\left(u\frac{\partial u}{\partial x}+v\frac{\partial u}{\partial y}\right)=-\frac{\partial P}{\partial x}+\frac{\partial\tau_{xx}}{\partial x}+\frac{\partial\tau_{yx}}{\partial y}+F_x$$

$$\rho\left(u\frac{\partial v}{\partial x}+v\frac{\partial v}{\partial y}\right)=-\frac{\partial P}{\partial y}+\frac{\partial\tau_{xy}}{\partial x}+\frac{\partial\tau_{yy}}{\partial y}+F_y \tag{5}$$

Energy Equation

In addition to the continuity and momentum equations, the energy equation is also employed in this study. This is because, in free convection flow, the density varies with temperature. The resulting energy equation is given as follows:

$$\left(u\frac{\partial T}{\partial x}+v\frac{\partial T}{\partial y}\right)=\alpha\frac{\partial^2 T}{\partial y^2}+\frac{Q_0}{\rho C_p}(T-T_\infty) \tag{6}$$

Wall Temperature

In this study, heat transfer occurs at the surface of the elliptic cylinder in free convection, giving rise to the wall temperature θ_w. Following [18], the temperature is defined as follows:

$$\theta_w=\frac{aq_w}{k(T_w-T_\infty)} \tag{7}$$

with

$$q_w=T-T_\infty \tag{8}$$

so that the following wall temperature expression is obtained

$$\theta_w=\frac{a(T-T_\infty)}{k(T_w-T_\infty)} \tag{9}$$

by defining

$$\theta=\frac{T-T_\infty}{T_w-T_\infty} \tag{10}$$

we obtained

$$\theta_w=\frac{a}{k}\theta \tag{11}$$

since $\theta_w\cong\theta$, so

$$\theta_w=\theta(x,y) \tag{12}$$

at the lower stagnation point, i.e. $x\approx 0$, the wall equation is obtained as follows:

$$\theta_w=\theta(0) \tag{13}$$

III. Mathematical Modelling

In this section, the mathematical formulation of the viscoelastic fluid flow over an elliptical cylinder is presented in a clear and systematic manner. All variables and parameters used in this study are defined in the Nomenclature section. The flow is assumed to be two-dimensional, incompressible, and laminar. Under these assumptions, the governing equations consist of the continuity, momentum, and energy equations which are presented in Eqs. (2), (5), and (6), respectively.

In Figure 1, the physical model of the viscoelastic fluid flow past an elliptical cylinder is illustrated. The figure also shows that the fluid flows from bottom to top, so that gravitational effects are present. The elliptical cylinder has axis lengths a and b. Here, A denotes the angle formed between the outward normal to the cylinder surface and the vertical line at the lower curved part of the cylinder. Based on this coordinate system, the following definitions can be introduced (see Cheng, 2012 [19]):

$$g_x=-g\sin A \tag{14}$$

with

$$\sin A=\frac{b}{a}\frac{\sin B}{(1-e^2\sin^2 B)^{\frac{1}{2}}} \tag{15}$$

the following equation is obtained

$$u\frac{\partial u}{\partial x}+v\frac{\partial u}{\partial y}=\nu\left[\frac{\partial^2 u}{\partial y^2}\right]+g\beta(T-T_\infty)\sin A-$$
$$\frac{k_0}{\rho}\left[u\left(\frac{\partial^3 u}{\partial x\partial y^2}\right)+v\frac{\partial^3 u}{\partial y^3}-\frac{\partial u}{\partial y}\left(\frac{\partial^2 u}{\partial y\partial x}\right)+\right.$$
$$\left.\frac{\partial u}{\partial x}\left(\frac{\partial^2 u}{\partial y^2}\right)\right] \tag{16}$$

In dimensional form, this can be written as

$$\bar{u}\frac{\partial\bar{u}}{\partial\bar{x}}+\bar{v}\frac{\partial\bar{u}}{\partial\bar{y}}=\nu\left[\frac{\partial^2\bar{u}}{\partial\bar{y}^2}\right]+g\beta(\bar{T}-\bar{T}_\infty)\sin A-$$
$$\frac{k_0}{\rho}\left[\bar{u}\left(\frac{\partial^3\bar{u}}{\partial\bar{x}\partial\bar{y}^2}\right)+\bar{v}\frac{\partial^3\bar{u}}{\partial\bar{y}^3}-\frac{\partial\bar{u}}{\partial\bar{y}}\left(\frac{\partial^2\bar{u}}{\partial\bar{y}\partial\bar{x}}\right)+\right.$$
$$\left.\frac{\partial\bar{u}}{\partial\bar{x}}\left(\frac{\partial^2\bar{u}}{\partial\bar{y}^2}\right)\right] \tag{17}$$

Boundary Conditions

The boundary conditions are defined as follows:
At the cylinder surface $(y=0)$:

$$u=0,\quad v=0,\quad \frac{\partial T}{\partial y}=-\frac{q_w}{k} \tag{18}$$

As $y\to\infty$:

$$u\to 0,\quad \frac{\partial u}{\partial y}\to 0,\quad T\to T_\infty \tag{19}$$

Non-Dimensional Formulation

To simplify the governing equations, the following dimensionless variables are introduced:

$$x^* = \frac{x}{L}, \quad y^* = \frac{y}{L}, \quad u^* = \frac{u}{U_\infty}, \quad v^* = \frac{v}{U_\infty} \tag{20}$$

$$\theta = \frac{T - T_\infty}{T_w - T_\infty} \tag{21}$$

Next, it is transformed into a non-dimensional form by introducing the appropriate non-dimensional variables, so that the following equation is obtained:

$$u\frac{\partial u}{\partial x} + v\frac{\partial u}{\partial y} = \frac{\partial^2 u}{\partial y^2} - K\left(\frac{\partial}{\partial x}\left(u\frac{\partial^2 u}{\partial y^2}\right) + v\frac{\partial^3 u}{\partial y^3} + \frac{\partial u}{\partial y}\frac{\partial^2 u}{\partial x \partial y}\right) + \theta \sin A \tag{22}$$

with boundary conditions:

$$u = v = 0, \quad \theta^{'} = -1 \quad for \quad y = 0$$

Stream Function Transformation

To automatically satisfy the continuity equation, a stream function ψ is introduced such that:

$$u = \frac{\partial \psi}{\partial y}, \quad v = -\frac{\partial \psi}{\partial x} \tag{23}$$

The stream function is expressed in the form:

$$\psi = x f(x, y), \quad \theta = \theta(x, y) \tag{24}$$

Substituting Eq. (10) into Eq. (8), the governing equation is transformed into a nonlinear partial differential equation:

$$\frac{\partial^3 f}{\partial y^3} + f\frac{\partial^2 f}{\partial y^2} - \left(\frac{\partial f}{\partial y}\right)^2 - x\left(\frac{\partial f}{\partial y}\frac{\partial^2 f}{\partial x \partial y} - \frac{\partial f}{\partial x}\frac{\partial^2 f}{\partial y^2}\right) + \theta \sin A - Kx\left(\frac{\partial^2 f}{\partial x \partial y}\frac{\partial^3 f}{\partial y^3} + \frac{\partial f}{\partial y}\frac{\partial^4 f}{\partial x \partial y^3} - \frac{\partial f}{\partial x}\frac{\partial^4 f}{\partial y^4} - \frac{\partial^2 f}{\partial y^2}\frac{\partial^3 f}{\partial x \partial y^2}\right) - K\left(2\frac{\partial f}{\partial y}\frac{\partial^3 f}{\partial y^3} - f\frac{\partial^4 f}{\partial y^4} - \frac{\partial^2 f}{\partial y^2}\frac{\partial^2 f}{\partial y^2}\right) = 0, \tag{25}$$

Reduced Equation at Stagnation Point

At the lower stagnation region ($x \approx 0$), Eq. (25) reduces to:

$$f^{'''} + ff'' - (f')^2 + \theta \sin A - K(2f'f''' - ff^{(4)} - (f'')^2) = 0, \tag{26}$$

with boundary conditions:

$$f(0) = f'(0) = 0, \quad \theta^{'}(0) = -1$$

$$f'(\infty) = 0 \quad {}''(\infty) = 0, \quad \theta(\infty) = 0, \tag{27}$$

IV. Numerical Solution

To ensure clarity and reproducibility, the present study employs an implicit finite difference method to discretize the governing equations. It is important to emphasize that the discretization is not directly applied to the original partial differential equations, but rather to the reduced nonlinear ordinary differential equations obtained in the stagnation region.

Discretized Governing Equations

The governing equation that is discretized is the reduced nonlinear momentum equation at the lower stagnation region, given by:

$$f''' + ff'' - (f')^2 + \theta \sin A - K\left(2f'f''' - ff^{(4)} - (f'')^2\right) = 0, \tag{28}$$

which is coupled with the energy equation:

$$\frac{d^2\theta}{d\eta^2} + Pr\, f\frac{d\theta}{d\eta} = 0. \tag{29}$$

To facilitate numerical treatment, the transformation

$$p = f', \quad f'' = p', \quad f''' = p'' \tag{30}$$

is introduced, reducing the higher-order nonlinear equation into a system of lower-order differential equations.

Spatial Discretization

The computational domain $\eta \in [0, \eta_{\max}]$ is discretized into N uniform grid points:

$$\eta_j = j\Delta\eta, \quad j = 0, 1, 2, \ldots, N. \tag{31}$$

All derivatives are approximated using second-order finite difference schemes evaluated implicitly at iteration level $(k+1)$:

First derivative:

$$\left(\frac{dp}{d\eta}\right)_j^{k+1} \approx \frac{p_{j+1}^{k+1} - p_{j-1}^{k+1}}{2\Delta\eta}, \tag{32}$$

Second derivative:

$$\left(\frac{d^2p}{d\eta^2}\right)_j^{k+1} \approx \frac{p_{j+1}^{k+1} - 2p_j^{k+1} + p_{j-1}^{k+1}}{\Delta\eta^2}. \tag{33}$$

Convergence and Stability Analysis

The convergence and stability of the numerical solution are closely related to the implicit finite difference method applied to the reduced nonlinear equation in Eq. (29). Since the governing equation involves higher-order derivatives and strong nonlinear viscoelastic effects through the parameter K, an iterative procedure is required to obtain a consistent solution. Convergence is achieved by updating the velocity gradient $p = f'$ and temperature θ iteratively until the maximum difference between successive iterations satisfies a prescribed tolerance. This ensures that the solution has reached a stable numerical state in the stagnation region.

The use of the implicit finite difference scheme, as introduced in Eq. (30), provides unconditional stability for the diffusive terms. This is particularly important for the present model, where the nonlinear coupling and higher-order terms may lead to numerical instability if treated using explicit schemes. The implicit formulation effectively stabilizes the solution and prevents divergence.

The stability and convergence of the method are further supported by the numerical results. As shown in Figures 2–7, the velocity and temperature profiles exhibit smooth and physically consistent behavior. In addition, the flow field and streamline patterns in Figure 8 do not show any spurious oscillations, while the temperature distribution in Figure 9 remains stable and symmetric. These observations confirm that the proposed numerical scheme produces stable and convergent solutions for the viscoelastic flow over the elliptical cylinder.

V. Result and Discussion

The mathematical model obtained in this study is solved using the implicit finite difference method and implemented numerically in MATLAB. According to [4], the parameters used for vortex-induced vibration (VIV) in the simulation of viscoelastic fluid flow are listed in Table 1.

TABLE I: Values of parameters for Vortex Induced Vibaration (VIV)

Parameters	**Values**
Reynolds number (Re)	$30 - 500$
Weissenberg number (We)	$0 - 10$
Viscosity ratio (β)	0.9
Reduced velocity (U_{re})	$3 - 12$
Structural damping ratio (ξ)	0
Mass ratio (m^*)	1.571

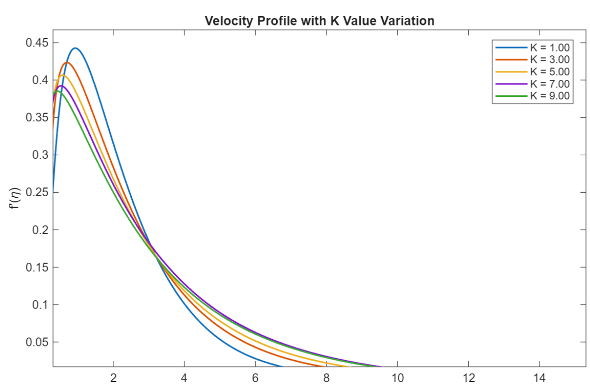

Fig. 2: Velocity Profiles with K Value Variation

In the Figure 2 illustrates the dimensionless velocity profile $f'(\eta)$ is shown as a function of the similarity variable η for several values of the viscoelastic parameter K. All curves start from $f'(0) = 0$ at the wall (no-slip condition), then increase to a maximum value, and subsequently decrease back towards zero as η becomes large, which reflects the typical behavior of a boundary layer. When K is small (for example $K = 1$), the peak of $f'(\eta)$ is higher, so the velocity near the wall is larger. As K increases ($K = 3, 5, 7, 9$), the peak of the curve decreases. This means that stronger viscoelastic effects hinder the fluid motion, so that the near-wall velocity is reduced and the velocity gradient (wall shear stress) becomes smaller. On the other hand, for larger η away from the wall, the curves with larger K lie slightly above those with smaller K, indicating that the momentum boundary layer becomes thicker because the velocity decreases more slowly with distance from the wall.

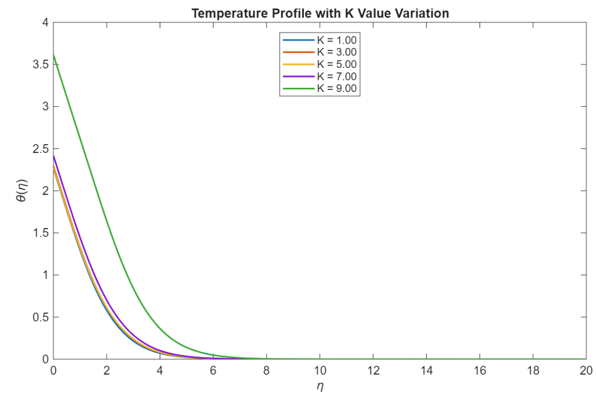

Fig. 3: Temperature Profiles with K Value Variation

The temperature profile in Figure 3 shows that $\theta(\eta)$ decreases from its maximum value at the wall ($\eta = 0$) towards zero as η increases, which illustrates the diminishing thermal influence of the surface on the fluid far from the wall. The variation of the viscoelastic parameter K is evident: for small K (for example $K = 1$) the temperature decreases rapidly so that the thermal boundary layer is relatively thin, whereas for large K (up to $K = 9$) the temperature near the wall is higher and decreases more slowly. This indicates that an increase in the viscoelastic property of the fluid (an increase in K) thickens the thermal boundary layer and at the same time reduces the temperature gradient at the wall. Since the convective heat transfer rate is proportional to $\theta'(0)$, it can be concluded that the larger the value of K, the less effective the heat transfer from the wall to the fluid becomes.

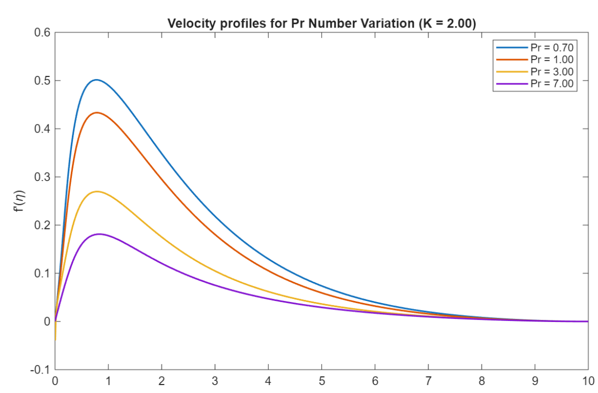

Fig. 4: Velocity Profiles with Prandtl Number Variation

The Figure 4 shows the dimensionless velocity profile $f'(\eta)$ as a function of the similarity variable η for several values of the Prandtl number Pr in a viscoelastic fluid with $K = 2$. All curves start from $f'(0) = 0$ at the wall (no-slip condition), then increase until they reach a maximum value at approximately

$\eta \approx 1$, and subsequently decrease gradually towards zero as η becomes large. This reflects the characteristic behavior of a boundary-layer flow over a solid surface. The influence of Pr variation is clearly seen in the peak height and the thickness of the momentum boundary layer. For small Pr (0.70 and 1.00), the velocity peak is higher and the curve decays more slowly, so the velocity remains significant up to larger values of η; this indicates a thicker momentum boundary layer. Conversely, as Pr increases (3.00 and 7.00), the maximum value of $f'(\eta)$ decreases and the curve approaches zero more rapidly, indicating that the velocity throughout the layer is reduced and the momentum boundary layer becomes thinner. Physically, an increase in Pr enhances the influence of momentum diffusivity relative to thermal diffusivity, so that the heating effect (and the buoyancy force driving the flow) becomes more localized near the wall, producing a weaker and thinner velocity profile.

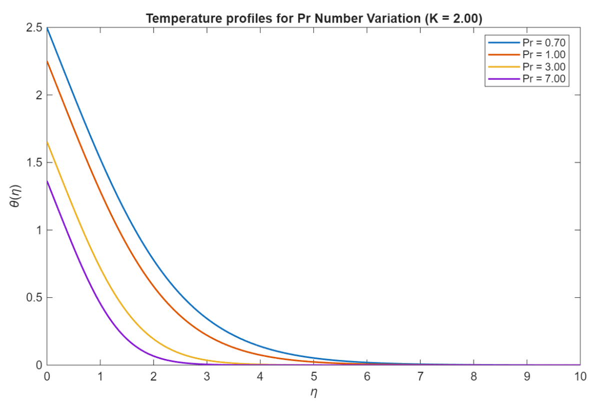

Fig. 5: Temperature Profiles with Prandtl Number Variation

Figure 5 shows the dimensionless temperature profile $\theta(\eta)$ for several values of the Prandtl number Pr in a viscoelastic fluid with $K = 2$. All curves start from a maximum value at the wall ($\eta = 0$) and decrease monotonically towards zero as η becomes large, in accordance with the behavior of a thermal boundary layer. The effect of varying Pr is clearly visible: when Pr is small (for example $\mathrm{Pr} = 0.7$), the values of $\theta(\eta)$ are higher throughout the domain and the decay is relatively slow, so the thermal boundary layer becomes thicker. Conversely, for larger Pr (3.00 and 7.00), the temperature curves lie lower and drop more rapidly to zero; this indicates that significant temperature exists only within a short distance from the wall, so the thermal boundary layer becomes thinner. Thus, an increase in the Prandtl number intensifies the temperature gradient near the wall and enhances the convective heat transfer rate, whereas a decrease in Pr leads to a wider spread of heat into the fluid.

The velocity profile in Figure 6 illustrates the effect of varying the aspect ratio of the elliptic cylinder (a/b) on the dimensionless velocity distribution $f'(\eta)$. In general, all curves start from the no-slip condition at the wall $(f'(0) = 0)$, then increase until they reach a maximum value at a similarity distance of about $\eta \approx 1$, and subsequently decrease gradually towards zero as η becomes larger. This pattern reflects the characteristic behavior of the momentum boundary-layer flow around the cylinder surface. The difference in ellipse shape

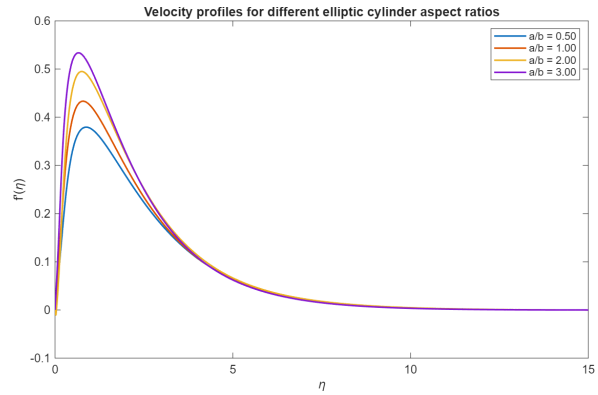

Fig. 6: Velocity Profiles for Different Elliptic Cylinder Aspect Ratios

has a clear influence on the peak velocity. For the aspect ratio $a/b = 0.5$, corresponding to a flatter geometry, the maximum value of $f'(\eta)$ is relatively small. As the aspect ratio increases to $a/b = 1.00$, 2.00, and 3.00, the peak of the velocity profile becomes higher, indicating that a more elongated (slender) elliptic cylinder produces a larger maximum velocity near the surface. However, in the region farther from the wall ($\eta \gtrsim 4$), the four curves almost coincide, so it can be concluded that the influence of aspect ratio variation is mainly significant in the near-surface region, while outside the momentum boundary layer the flow recovers a nearly identical character for all values of a/b.

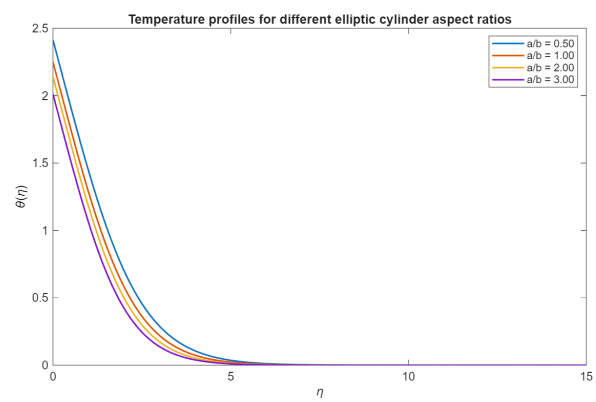

Fig. 7: Temperature Profiles for Different Elliptic Cylinder Aspect Ratios

Figure 7 shows the dimensionless temperature profile $\theta(\eta)$ for several aspect ratios of an elliptic cylinder (a/b). All curves start from a maximum value at the wall ($\eta = 0$) and decrease monotonically, approaching zero as η increases, which represents the behavior of the thermal boundary layer around the cylinder surface. It is observed that for $a/b = 0.50$ (a flatter ellipse), the values of $\theta(\eta)$ are higher and decay more slowly, so the thermal boundary layer becomes thicker. As the aspect ratio increases to $a/b = 1.00$, 2.00, and 3.00, the temperature near the wall decreases and the curves drop to zero more rapidly. This indicates that a more elongated elliptic cylinder yields a thinner thermal boundary layer and a steeper temperature gradient at the wall. Thus, an increase in the aspect ratio a/b tends to enhance the convective heat transfer rate from the cylinder surface to the surrounding fluid, while its influence becomes increasingly weak in the region far from the wall where all curves nearly coincide.

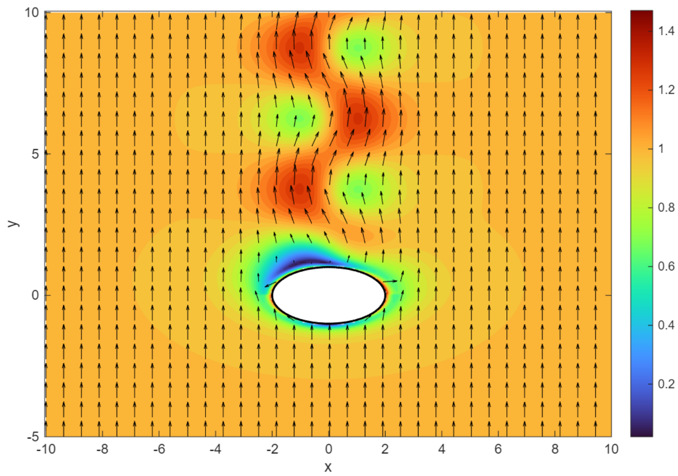

(a)

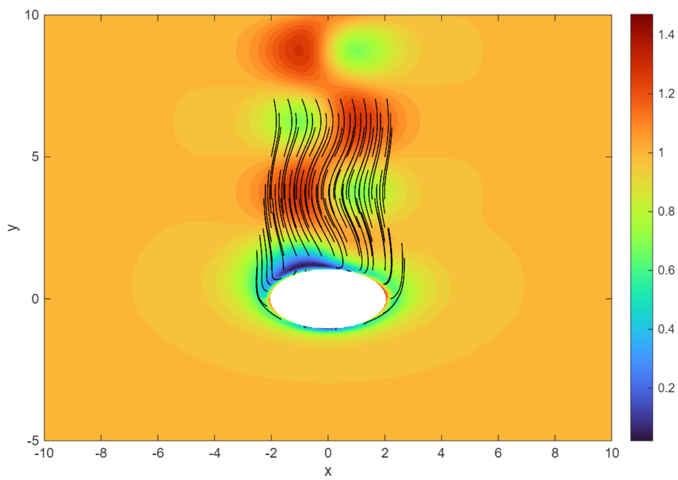

(b)

Fig. 8: (a) Velocity distribution around the elliptic cylinder, (b) Streamlines around the elliptic cylinder

The Figure 8(a) shows the velocity field indicates that the viscoelastic flow over the elliptical cylinder is characterized by a nearly uniform upstream velocity of approximately $U \approx 1.0$–1.2. As the fluid approaches the frontal surface, the velocity decreases significantly to about $U \approx 0.2$–0.4, forming a distinct stagnation region due to local pressure buildup. Along the lateral sides of the cylinder, the flow accelerates and reaches peak values of approximately $U \approx 1.3$–1.5, driven by geometric constriction and momentum redistribution. In the downstream region, the wake exhibits modulated velocity bands ranging from $U \approx 0.6$–1.4, indicating variations in flow intensity without the formation of a strong periodic vortex street. The absence of large velocity fluctuations and the relatively smooth transition in magnitude confirm that viscoelastic effects effectively damp flow instabilities, suppress vortex shedding, and promote a more stable wake structure behind the elliptical cylinder.

The Figure 8(b) shows the velocity field and streamlines illustrate the behavior of viscoelastic flow over an elliptical cylinder, with a predominantly upward flow exhibiting a nearly uniform upstream velocity ($U \approx 1.0$–1.2). As the fluid approaches the frontal surface, a significant deceleration occurs ($U \approx 0.2$–0.4), forming a stagnation region associated with local pressure buildup. The streamlines clearly demonstrate flow deflection along the lateral sides of the cylinder, satisfying the no-penetration boundary condition. Along these sides, the flow accelerates and reaches peak velocities of approximately $U \approx 1.3$–1.5 due to geometric constriction. In the downstream region, the wake exhibits modulated velocity bands ($U \approx 0.6$–1.4) accompanied by mild oscillatory streamline patterns, indicating the presence of weak vortex-like structures. However, the absence of a well-defined periodic vortex street suggests that viscoelastic effects effectively damp flow instabilities, suppress coherent vortex shedding, and promote a more stable and controlled wake structure behind the elliptical cylinder.

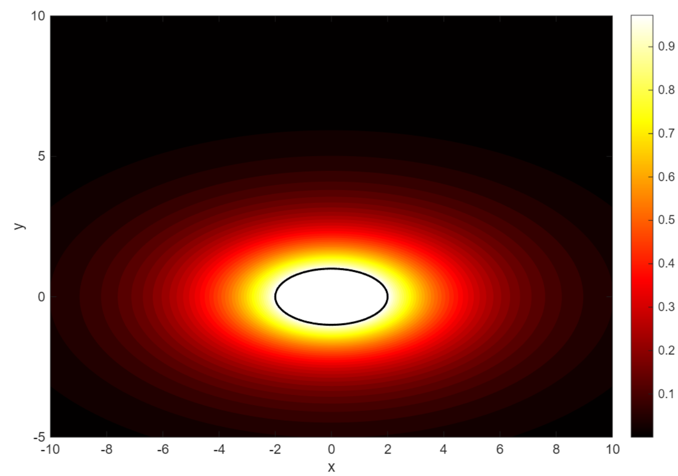

Fig. 9: Temperature Distribution (Upward Flow)

The Figure 9 shows the dimensionless temperature distribution around an elliptic cylinder in an upward viscoelastic flow for $Pr = 1.5$. The white region represents the solid cylinder, while the coloured contours indicate the temperature field, with bright yellow/white corresponding to the highest nondimensional temperature and dark red/black to the lowest values. The maximum temperature occurs at the cylinder surface, and the isotherms form nearly concentric ovals around the body, indicating that heat diffuses from the heated cylinder into the surrounding fluid. Close to the surface, the colour changes very rapidly, forming a thin bright layer. This indicates a steep temperature gradient at the wall, which corresponds to a relatively high local heat flux and a thin thermal boundary layer. As the distance from the cylinder increases, the isotherms become more widely spaced and the temperature decreases smoothly toward the ambient value; the far-field region is almost uniform and close to zero nondimensional temperature, meaning the influence of the heated cylinder becomes negligible there. The distribution is symmetric with respect to both axes, showing that for this configuration the thermal field is dominated by diffusion and weakly affected by convection in the vertical direction. From a VIV-mitigation viewpoint, such a smooth and symmetric thermal field suggests that buoyancy-induced forces are well distributed around the cylinder and do not introduce strong asymmetric thermal plumes that could enhance flow unsteadiness or amplify vortex-induced vibrations.

The viscoelastic parameter K, which is physically associated with the Weissenberg number (We), represents the strength of elastic effects in the flow, as summarized in Table 1. An increase in K (or We) in Figure 2 leads to a reduction in the peak velocity $f'(\eta)$ near the wall and a weakening of the velocity gradient, indicating reduced wall shear stress and a thickening of the momentum boundary layer. This behavior is consistent with Figure 8, where the wake becomes smoother and vortex shedding is effectively suppressed. In contrast, the variation of the Prandtl number Pr in Figure 4, also listed in Table 1, shows that low Pr produces higher velocity profiles and thicker boundary layers, whereas higher Pr reduces the velocity magnitude and thins the boundary layer due to enhanced convective effects governed by the Reynolds number (Re). In this context, Re and Pr are intrinsically coupled in determining the balance between convective and diffusive transport, where increasing Re intensifies convection while Pr modulates thermal diffusion. The temperature distributions (Figures 3 and 5) further support this relationship: increasing K (or We) thickens the thermal boundary layer and reduces temperature gradients, while increasing Pr enhances temperature gradients and heat transfer. Overall, as indicated by the parameter ranges in Table 1, Re strengthens convective transport and wake formation, whereas We acts as a stabilizing mechanism that smooths the velocity and temperature fields.

Based on the MATLAB results, future studies should further explore the roles of the Reynolds number (Re) and Weissenberg number (We) in wake dynamics. At moderate Re, flow acceleration and wake formation indicate instability onset, while increasing We smooths the wake and suppresses vortex shedding. Extending the model to unsteady and three-dimensional simulations, along with quantifying vortex shedding, drag, and flow-induced vibrations, is essential to better understand their interplay in controlling flow stability. Such analysis would provide deeper insight into the balance between inertial and elastic effects in viscoelastic flows.

VI. CONCLUSIONS

Based on the present numerical analysis, it is concluded that viscoelasticity exerts a dominant control over the momentum and thermal boundary-layer structures around an elliptical cylinder. An increase in the viscoelastic parameter K markedly suppresses the peak velocity $f'(\eta)$, reduces wall shear stress, and significantly thickens both momentum and thermal boundary layers, thereby attenuating near-wall gradients responsible for vortex generation. This behavior is further reflected in the slower decay of the temperature profile $\theta(\eta)$ and the reduction of wall heat flux, confirming the dissipative role of viscoelasticity in weakening flow instabilities. In parallel, the Prandtl number Pr governs the spatial localization of transport phenomena, where higher Pr compresses boundary layers and intensifies wall gradients, while lower Pr promotes more diffused profiles. The geometric effect, represented by the aspect ratio a/b, is primarily confined to the near-wall region, with flatter configurations reducing peak velocities and enhancing boundary-layer thickness, whereas more slender geometries amplify velocity peaks and sharpen thermal gradients. From a control perspective, the combined manipulation of K, Pr, and a/b provides an effective passive strategy for mitigating Vortex-Induced Vibration (VIV) by weakening shear layers and reducing the energy available for vortex shedding.

Future work should investigate the coupled effects of the Reynolds number (Re) and Weissenberg number (We) on flow stability over wider parameter ranges. Extending the model to unsteady and three-dimensional cases, along with quantitative evaluation of vortex shedding, drag, and flow-induced vibrations, will enhance the applicability of the present results.

ACKNOWLEDGMENT

The authors would like to express their sincere gratitude to Universitas PGRI Adi Buana Surabaya for the financial support provided for this research. This support made it possible to conduct the numerical simulations and analysis of viscoelastic flow and vortex-induced vibration presented in this work. The authors also appreciate the academic environment and facilities that have contributed to the completion of this study.

REFERENCES

[1] Varela, J., and Pinelli, A. (2019). Effects of elasticity on vortex shedding in viscoelastic flow around a cylinder. Physics of Fluids, 31(6), 063101.
[2] Khalili, M., and Hosseini, S. (2021). Numerical study of viscoelastic fluid flow around bluff bodies. Computers and Fluids, 224, 104974.
[3] Karlson, N., Nita, R., and Vaidya, P. (2020). Numerical computations of vortex formation length in flow past an elliptical cylinder.
[4] Umang N. Patel and Jonathan P. Rothstein and Yahya Modarres-Sadeghi (2024), Viscoelasticity in the flow suppresses one- and two-degree-of-freedom vortex-induced vibrations of a cylinder, Physical Review Fluids, Vol. 9, No. 11, pp. 113301, 10.1103/PhysRevFluids.9.113301. https://www.sciencedirect.com/science/article/pii/S037702571930196X.
[5] Jia Wang and Hang Xu (2022), Active control of flow past an elliptic cylinder using an artificial neural network trained by deep reinforcement learning, Applied Mathematics and Mechanics, Vo/ 43, pp. 1921–1934, 10.1007/s10483-022-2940-9.
[6] Junwei Li and Benmou Zhou (2022), Vortex shedding, flow separation, and drag coefficient in the flow past an ellipsoid of different aspect ratios at moderate Reynolds number, AIP Advances, Vo. 12, pp. 055202, 10.1063/5.0090735.
[7] Umang N. Patel and Jonathan P. Rothstein and Yahya Modarres-Sadeghi (2023), Forced oscillations of a cylinder in the flow of viscoelastic fluids, Journal of Fluid Mechanics, Vol. 975, pp. A28, 10.1017/jfm.2023.861.
[8] Faheem Hamid and C. Sasmal (2023), Significant influence of fluid viscoelasticity on flow dynamics past an oscillating cylinder, arXiv preprint.
[9] Xinru Wang and Jianxun Zhu and Lars E. Holmedal and Dag Myrhaug and Hong Wang (2025), Numerical investigation of oscillatory flow regimes around an elliptic cylinder at low Keulegan–Carpenter and Reynolds numbers, Physical Review Fluids, Vo. 10, pp. 024702, 10.1103/PhysRevFluids.10.024702.
[10] Yuxin Li and Bo Li and Tian Li and Yuanzhao Zhang (2024), Numerical study on the flow around an elliptic cylinder with different aspect ratios in the subcritical regime using large eddy simulation, Physics of Fluids, Vol. 36, pp. 015154, 10.1063/5.0187134.
[11] Yuxin Li and Bo Li and Tian Li and Yuanzhao Zhang (2024), Numerical study on the flow around an elliptic cylinder with different aspect ratios in the subcritical regime using large eddy simulation, Physics of Fluids, Vo. 36, pp. 015154, 10.1063/5.0187134.

[12] Jia Wang and Hang Xu (2025), Numerical investigation of oscillatory flow regimes around an elliptic cylinder at low Keulegan–Carpenter and Reynolds numbers, Physical Review Fluids, Vol. 10, pp. 024702, 10.1103/PhysRevFluids.10.024702.

[13] Xiong, Yongliang and Peng, Sai and Zhang, Mengqi and Yang, Dan (2019), Numerical study on the vortex-induced vibration of a circular cylinder in viscoelastic fluids, Journal of Non-Newtonian Fluid Mechanics, Vo. 272, pp. 104170.

[14] Pieter R. Boersma and Jonathan P. Rothstein and Yahya Modarres-Sadeghi (2024), Suppression of vortex-induced vibrations of a cylinder in inertial-elastic flow, Journal of Non-Newtonian Fluid Mechanics, Vol. 324, pp. 105170, 10.1016/j.jnnfm.2023.105170.

[15] Justin Antony and Ranjith Maniyeri (2022), Numerical Simulation of Flow Past Elliptic Cylinder Using Smoothed Particle Hydrodynamics, Lecture Notes in Mechanical Engineering,Springer, pp. 205–214, isbn: 978-981-19-3379-0.

[16] Prateek Gupta and Sibasish Panda and Akhilesh Kumar Sahu and Deepak Kumar (2022), Effect of confinement on flow around a rotating elliptic cylinder in laminar flow regime, Fluids Engineering, Vol. 145, pp. 101301, 10.1115/1.4062621.

[17] Basuki Widodo, Isnainatul Mayagrafinda, Dieky Adzkiya (2022), Magnetohydrodynamics nano fluid flows through a vertical porous cylinder, AIP Conference Proceedings, Vol. 2641 (1), https://pubs.aip.org/aip/acp/article-abstract/2641/1/030003/2831064/Magnetohydrodynamics-nano-fluid-flows-through-a.

[18] Hossain, M. Anwar and Khanafer, K. and Vafai, K. and others (2001), The effect of radiation on free convection flow of fluid with variable viscosity from a porous vertical plate, International Journal of Thermal Sciences, Vol. 40 (2), pp. 115–124, 10.1016/S1290-0729(00)01200-X.

[19] Cheng, C.-Y. (2012), Free Convection of Non-Newtonian Nano Fluids about a Vertical Truncated Cone in a Porous Medium, International Communications in Heat and Mass Transfer, Vo. 39, pp. 1348–1353, 10.1016/j.icheatmasstransfer.2012.08.004.